Journal of Volcanology and Geothermal Research 198 (2010) 205–216

Contents lists available at ScienceDirect

Journal of Volcanology and Geothermal Research

journal homepage: www.elsevier.com/locate/jvolgeores

Effects of caldera collapse on magma decompression rate: An example from the 1800 ^{14}C yr BP eruption of Ksudach Volcano, Kamchatka, Russia

Benjamin J. Andrews *, James E. Gardner

Department of Geological Sciences, Jackson School of Geosciences, 1 University Station C1100, The University of Texas at Austin, Austin, TX 78712-0254, United States

ARTICLE INFO

Article history:
Received 11 February 2010
Accepted 20 August 2010
Available online 21 September 2010

Keywords:
caldera
magma decompression
experimental petrology
Kamchatka
eruption conduit

ABSTRACT

Caldera collapse changes volcanic eruption behavior and mass flux. Many models of caldera formation predict that those changes in eruption dynamics result from changes in conduit and vent structure during and after collapse. Unfortunately, no previous studies have quantified or described how conduits change in response to caldera collapse. Changes in pumice texture coincident with caldera formation during the 1800 ^{14}C yr BP KS_1 eruption of Ksudach Volcano, Kamchatka, provide an opportunity to constrain magma decompression rates before and after collapse and thus estimate changes in conduit geometry. Prior to caldera collapse, only white rhyodacite pumice with few microlites and elongate vesicles were erupted. Following collapse, only gray rhyodacite pumice containing abundant microlites and round vesicles were erupted. Bulk compositions, phase assemblages, phenocryst compositions, and geothermometry of the two pumice types are indistinguishable, thus the two pumice types originated from the same magma. Geothermobarometry and phase equilibria experiments indicate that magma was stored at 100–125 MPa and 895 ± 5 °C prior to eruption. Decompression experiments suggest microlite textures observed in the white pumice require decompression rates of >0.01 MPa s^{-1}, whereas the textures of gray pumice require decompression at ~0.0025 MPa s^{-1}. Balancing those decompression rates with eruptive mass fluxes requires conduit size to have increased by a factor of ~4 during caldera collapse. Slower ascent through a broader conduit following collapse is also consistent with the change from highly stretched vesicles present in white pumice and to round vesicles in gray pumice. Numerical modeling suggests that the mass flux and low decompression rates during the Gray phase can be accommodated by the post-collapse conduit developing a very broad base and narrow upper region.

1. Introduction

Calderas form during voluminous eruptions, when a volcanic edifice collapses into an emptying magma chamber. Observations of modern eruptions and interpretations of ancient deposits indicate that collapse is frequently accompanied by increased mass flux and a change from dominantly buoyant, Plinian behavior to generation of dominantly non-buoyant pyroclastic flows (Sigurdsson and Carey, 1989; Scott et al., 1996; Andrews et al., 2007). Such observations have been incorporated into models of caldera formation that predict both increased mass flux and pyroclastic flow generation after collapse (Bacon, 1983; Druitt and Sparks, 1984; Hildreth and Mahood, 1986; Suzuki-Kamata et al., 1993; Wilson and Hildreth, 1997; Lipman, 2000). Those models, primarily developed for eruptions of >30 km^3 magma (dense rock equivalent, DRE) describe initial activity at a single vent, initiation of collapse after a small (~10%) fraction of magma is erupted, and the opening of multiple or ring vents during and after collapse. The increased number and size of those vents, and the conduits that supply them, is believed to accommodate the increased mass flux (e.g., Wilson and Hildreth, 1997). Contrary to such general models, caldera collapse likely occurs relatively late in eruptions of more modest volume (<10 km^3 magma, DRE), after ~3/4 of the magma or more has been expelled (Gardner and Tait, 2000; Roche and Druitt, 2001; Andrews et al., 2007). Interestingly, although pyroclastic flow generation may increase following caldera collapse in those smaller eruptions, mass flux does not necessarily increase (Gardner and Tait, 2000; Andrews et al., 2007).

Absent from most studies of caldera-forming eruptions are quantitative descriptions of changes in conduit geometry following collapse or thorough examinations of the effects of collapse on magma ascent rate. Because mass flux is the product of conduit geometry and magma ascent rate, understanding why mass flux changes during an eruption requires knowledge of at least one of those other parameters. Moreover, because magma ascent may be driven by buoyancy, overpressure in the chamber, or some combination of those forces, and is strongly affected by conduit size (Druitt and Sparks, 1984; Jaupart, 2000; Mastin and Ghiorso, 2000; Mastin, 2002), balancing mass flux, conduit geometry, and magma ascent rate can provide insight regarding changes in subsurface structure following caldera collapse.

Here, we quantify changes in decompression and ascent rate during caldera collapse and infer changes in conduit structure by comparing

* Corresponding author. Earth and Planetary Science Department, 307 McCone Hall, University of California, Berkeley, Berkeley, CA 94720-4767, United States.
E-mail address: andrews@eps.berkeley.edu (B.J. Andrews).

0377-0273/$ – see front matter © 2010 Elsevier B.V. All rights reserved.
doi:10.1016/j.jvolgeores.2010.08.021

textures of decompression experiments with measured changes in groundmass textures within pumice erupted during the KS_1 caldera-forming eruption of Ksudach volcano. That eruption, in ~1800 ^{14}C yr BP, occurred in four phases, and caldera collapse happened after ~65% of the total volume erupted in this eruptive sequence was ejected. Mass flux remained relatively constant or decreased slightly after collapse began (Andrews et al., 2007). Our work shows that a change in pumice color from white to gray coincident with caldera collapse (Andrews et al., 2007) reflects changes in vesicle texture and increased microlite content, and those differences reflect a reduced decompression rate. Interestingly, the balance between mass flux, conduit size, and decompression rate suggests that although the conduit base widened significantly following collapse, upper regions of the conduit narrowed.

1.1. KS_1 eruption background

The ~1800 ^{14}C yr BP KS_1 eruption deposited ~8.5 km^3 of compositionally uniform rhyodacite magma (DRE) along much of the length of the Kamchatka Peninsula (Fig. 1) (Braitseva et al., 1996; Andrews et al., 2007). A complete description of the eruption and its deposits can be found in Andrews et al. (2007). In summary, the eruption can be subdivided into four phases, Initial, Main, Lithic, and Gray, based on mass flux, lithic concentration, and pumice color. During the Initial phase, mass flux doubled from 5×10^7 to 10^8 kg s^{-1} and 1–1.4 km^3 of magma (DRE) was erupted. Mass flux during the Main phase increased to 2–6$\times10^8$ kg s^{-1} and 4.5–5.5 km^3 of magma (DRE) was deposited. Although the Lithic phase deposits are volumetrically small, ~0.2 km^3 magma (DRE), mass flux remained relatively high during this phase, 1–4$\times10^8$ kg s^{-1}. Gray phase mass flux did not change significantly from the previous two phases, remaining at 2–3$\times10^8$ kg s^{-1}, and 2–2.5 km^3 of magma (DRE) was erupted. All mass fluxes were calculated using isopleth maps of maximum lithic size (Carey and Sparks, 1986).

Lithic eruption rates and the concentration of lithics in fall deposits vary substantially with the eruption phases. During the Initial phase, approximately 0.2 km^3 of accidental lithics were erupted at rates of 0.5–2$\times10^7$ kg s^{-1}, resulting in fall deposits with up to ~20 wt.% lithics. The eruption rate of lithics during most of the Main phase was 1–2$\times10^7$ kg s^{-1}, as nearly 0.5 km^3 of lithics were ejected to produce fall deposits with generally <10 wt.% lithics. Lithic phase fall deposits contain >50 wt.% lithics, reflecting the eruption of ~0.3 km^3 of lithics at rates of 2–7$\times10^7$ kg s^{-1}. Lithic eruption rates during the Gray phase decreased to 0.5–1$\times10^7$ kg s^{-1}, as approximately 0.25 km^3 of lithics were erupted, resulting in fall deposits with ~10 wt.% lithics.

Collapse of Ksudach Caldera V likely began during the Lithic phase (Andrews et al., 2007). The deposits represent eruption of a single magma and pumice color thus indicates the timing of eruption relative to caldera collapse: careful and thorough inspection shows that no gray pumice were erupted before and no white pumice after the start of the Gray phase (Andrews et al., 2007). In addition, caldera formation caused an increase in the eruption of pyroclastic flows: during the Main phase, ~1/3 of the eruptive mass flux fed flows, whereas ~2/3 of the Gray phase mass flux supplied pyroclastic flows (Andrews et al., 2007).

2. Experimental and analytical methods

Samples of pumice were collected from near the southern caldera rim and at locations ~11 km NNE and ~50 km N of the caldera (Fig. 1). Bulk chemical analyses were collected for Initial phase pumice 02IPE45 and Gray phase pumice 02IPE18. Thin sections were made of those samples and additional thin sections were prepared from Initial, Main, Lithic, and Gray phase pumice for glass, phenocryst, and textural analysis. A portion of sample 02IPE45 was gently crushed to a <50 μm powder for use as starting material in phase equilibria and decompression experiments.

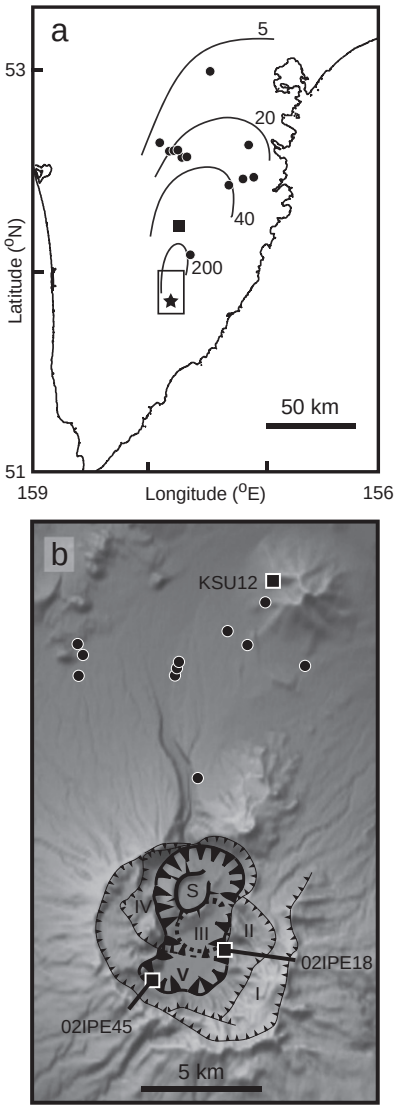

Fig. 1. Location of Ksudach volcano in southern Kamchatka. a) Cumulative deposits from the KS_1 eruption are dispersed over much of Kamchatka along a NNE depositional axis (Andrews et al., 2007). b) The 1800 ^{14}C KS_1 eruption formed Caldera V, the youngest of five nested calderas (I–V) in the Ksudach massif; recent activity has been focused at Shtuybel cone, S (after Braitseva et al., 1996). Sample sites from Andrews et al. (2007) are shown with black circles, locations of samples used in this study are indicated by black boxes (location KSU23 in a, and locations 02IPE18, 02IPE45, and KSU12 in b).

Phase equilibria experiments were prepared by sealing powder in 2-mm O.D. $Ag_{70}Pd_{30}$ tubing with sufficient deionized H_2O to ensure that all experiments were water saturated ($P_{total}=P_{H2O}$). Those experiments were conducted in externally heated Waspalloy pressure vessels with nickel filler rods and pressurized with H_2O at a range of temperatures and pressures (Table 1). Oxygen fugacity during the experiments is estimated at approximately one log unit (±0.5) above the Ni–NiO (NNO) buffer curve. All experiments were quenched by first cooling the pressure vessels with forced air, and then immersing them in water. After each experimental run, the sample was mounted in epoxy on thin sections and polished for analysis. Stable phases were identified using a petrographic microscope and electron microprobe.

Two high-temperature phase equilibria experiments, K-10 and K-22B, were conducted in an externally heated TZM pressure vessel pressurized with argon and ~0.1 MPa methane to minimize hydrogen migration. Oxygen fugacity for that experiment was fixed at NNO by loading Ni metal and NiO powders into a 4-mm $Ag_{70}Pd_{30}$ tube also loaded with a 2-mm

Table 1
Phase equilibria experimental conditions. Initial material for experiments was either crushed white pumice 02IPE45, or a previously run experiment. Stable mineral phases are indicted by ox (Fe–Ti oxides), px (pyroxene), or plg (plagioclase). Plagioclase composition is indicated by anorthite content, for example An_{30} denotes plagioclase with 30 mol% anorthite; uncertainties in anorthite content are estimated to be 1 mol%.

Run	Initial material	Duration(h)	P_i(MPa)	T(°C)	Stable phases
K-1R	02IPE45	92	100	900	gl, ox, px, plg (An_{43})
K-2	02IPE45	96	100	750	gl, ox, px, plg
K-3	K-1R	96	100	800	gl, ox, px, plg (An_{30})
K-4	K-2	96	100	800	gl, ox, px, plg (An_{29})
K-5	K-1R	96	100	850	gl, ox, px, plg (An_{35})
K-6	K-2	96	100	850	gl, ox, px, plg (An_{38})
K-7	K-1R	96	100	875	gl, ox, px, plg (An_{35})
K-8	K-2	96	100	875	gl, ox, px, plg (An_{37})
K-10	02IPE45	96	100	950	gl, ox, px
K-11A	K-1R	95	200	900	gl, ox, px
K-11B	K-1R	95	200	900	gl, ox
K-12A	K-6	236	200	850	gl, ox, px
K-12B	K-1R	236	200	850	gl, ox, px
K-13	K-7	233	100	850	gl, ox, px, plg (An_{36})
K-14	02IPE45	162	50	900	gl, ox, px, plg (An_{37})
K-15	02IPE45	364	50	850	gl, ox, px, plg (An_{31})
K-16	K-11A	389	250	850	gl, ox, px
K-17	K-1R	294	150	875	gl, ox, px
K-18A	K-1R	183	200	875	gl, ox, px
K-18B	K-8	183	100	875	gl, ox, px, plg (An_{40})
K-19	02IPE45	120	100	900	gl, ox, px, plg (An_{45})
K-20	02IPE45	209	50	875	gl, ox, px, plg (An_{36})
K-21	K-14	141	100	900	gl, ox, px, plg (An_{38})
K-22A	K-15	96	100	850	gl, ox, px, plg (An_{30})
K-22B	K-19	118	100	925	gl, ox, px
K-23	K-11A	94	150	825	gl, ox, px, plg (An_{36})
K-24	02IPE45	96	150	825	gl, ox, px, plg (An_{37})
KD-8	K-1R	96	75	900	gl, ox, px, plg (An_{39})
KD-9	K-19	96	75	875	gl, ox, px, plg (An_{36})

$Ag_{70}Pd_{30}$ tube containing the sample and sufficient deionized water to ensure saturation of the experiment. The presence of both Ni and NiO at the conclusion of the experiment indicates oxygen fugacity was fixed during the run.

To verify phase stabilities, three pairs of reversal experiments were conducted to verify phase stabilities: for a given pressure and temperature, aliquots of one sample equilibrated at higher pressure and/or temperature and one at lower pressure and/or temperature, were reloaded and sealed in 2-mm O.D. $Ag_{70}Pd_{30}$ tubes with sufficient deionized water for saturation and run at the given conditions. The presence of the same phase assemblages and phase compositions in the two experiments is considered to indicate phase stability at the given conditions. All reversal experiments were conducted in Waspalloy pressure vessels with nickel filler rods pressurized with H_2O.

2.1. Decompression experiments

Starting materials for decompression experiments were prepared by loading crushed pumice into 2-mm O.D. $Ag_{70}Pd_{30}$ tubes with sufficient deionized H_2O to ensure that all experiments were water saturated ($P_{total} = P_{H2O}$). Starting materials for decompression experiments were prepared by annealing the sample in an externally heated Waspalloy pressure vessel pressurized with H_2O at starting P–T conditions for at least 96 h. Decompression experiments were begun before completion of the experimental phase diagram, and thus groups of experiments were decompressed from different initial conditions (Table 2). An aliquot of each starting material was prepared for thin section analysis of microlite textures at initial P–T conditions. Other aliquots of each starting material were reloaded into $Ag_{70}Pd_{30}$ tubes for decompression and held at initial temperature and pressure (+4 MPa) for 2 h. Decompression was accomplished in multiple increments of 5 MPa using a hand operated pressure intensifier; we estimate each pressure drop occurred in less than 5 s. The decompression rate was calculated by dividing that 5 MPa decrease by the time between pressure drops; for example, lowering pressure every 1000 s results in a decompression rate of 0.005 MPa s^{-1}. All samples were decompressed to 20 MPa and quenched with forced air and then immersed in water. That final pressure approximates the pressure estimated from bulk vesicularities and initial water contents of the white and gray pumice assuming closed-system degassing. Pressure and vesicularity are related with the expression

$$Ves = \frac{\frac{X_{v,P}RT}{P}}{\frac{X_{v,P}RT}{P} + \Sigma X_i V_i + X_{H2O,P} V_{H2O,P}} \quad (1)$$

in which, Ves is the volume fraction of vesicles, R is the universal gas constant, T is temperature in K, X_i and V_i are the anhydrous mole fractions and molar volumes of all oxide species in the melt (from Spera, 2000), $X_{H2O,P}$ and $V_{H2O,P}$ are the mole fraction and molar volume of H_2O dissolved in the melt at pressure P, as calculated using the method of Moore et al. (1998). The number of moles of H_2O vapor at a given pressure, $X_{v,P}$, is calculated from the difference of the initial mole fraction of H_2O dissolved in the melt and $X_{H2O,P}$.

2.2. Compositional analyses

Mineral and glass compositions were analyzed with JEOL JXA-8600, Cameca SX-50, and Cameca SX-100 electron microprobes at the University of Texas at Austin, the University of Alaska Fairbanks, and the University of California at Davis Departments of Geological Sciences. All analyses were conducted using a 15 kV, 10 nA beam; mineral analyses were conducted with a focused beam, whereas glass analyses were conducted with a 10-μm defocused beam. Analyses were processed using JEOL, Probe for Windows, and Cameca software. Sodium migration in glasses was monitored and corrected using the volatile correction program within Probe for Windows. Comendite glass KN-18 was used to monitor any drift during glass analyses.

Crystals from lightly crushed white (02IPE45) and gray (02IPE18) pumice were selected for melt inclusion analysis. Crystals containing melt inclusions were mounted in orthodontic resin, glued to slides with thermoadhesive Crystalbond® 509, and polished until the inclusions of interest were intersected. The Crystalbond® 509 was then reheated, allowing the crystals to be flipped and reattached to the slide. The second sides of the crystals were then polished so that melt inclusions were doubly-intersected and doubly-polished. Immediately prior to FTIR analysis, the orthodontic resin surrounding each crystal was dissolved with acetone; the crystals were then cleaned with ethanol.

Melt inclusion compositions were measured with Fourier transform infrared spectroscopy (FTIR) and then electron microprobe. Those samples were analyzed with a ThermoElectron Nicolet Nexus 670 FTIR in the Department of Geological Sciences at the University of Oregon. All analyses were conducted using transmission of white light through a KBr window. For each spectra, 250 to 1000 scans were collected with a resolution of 4 cm^{-1}. FTIR spectra were examined at 3550 cm^{-1} wavenumbers for total H_2O. No CO_2 was detected in any inclusion. Measured IR absorbances were converted to water concentrations using the methods of Stolper (1982), Newman et al. (1986), and Zhang et al. (1997). Absorptivity of 76 L mol^{-1} mm^{-1} was used for the 3550 cm^{-1} absorption band. Inclusion thicknesses were measured by mounting the crystals on a pin and examining them on edge, in oil, under a microscope; the error associated with this technique is ±2 μm.

2.3. Textural analyses

Bulk vesicularities of samples were measured using the method of Gardner et al. (1996). The wet and dry masses of 15 ~1-cm diameter pumice from both the Main and Gray phase fall samples KSU-23H and

Table 2
Decompression experimental conditions. Initial material for experiments was either crushed white pumice 02IPE45, or a previously run experiment. Stable mineral phases are indicted by ox (Fe–Ti oxides), px (pyroxene), or plg (plagioclase). Plagioclase composition is indicated by anorthite content, for example An_{30} denotes plagioclase with 30 mol% anorthite; uncertainties in anorthite content are estimated to be 1 mol%. Crystallinity of microlite phases present in decompression experiments, but in concentrations <0.1 vol.% are denoted tr. Number densities, N_V, are presented in mm^{-3}. All decompression experiments were quenched at 20 MPa. Uncertainties in N_V are 1 standard deviation. Experiments marked with an asterisk (e.g., KD-1*) were used as starting material for subsequent experiments, and hence have no decompression rate.

Run	Initial material	P_i (MPa)	T (°C)	Stable phases	dP/dt (MPa/s)	Fe–Ti oxides		Pyroxene		Plagioclase	
						vol.%	N_V	vol.%	N_V	vol.%	N_V
KD-1*	02IPE45	150	890	gl, ox, px	–	*tr*	$3.6\times(\pm2)10^4$	0.3	$1.3(\pm0.5)\times10^3$	0	0
KD-2	KD-1	150	890		0.05	0.1	$1.1\times(\pm1)10^6$	0.1	$6.5(\pm3)\times10^4$	0	0
KD-3	KD-1	150	890		0.01	0.3	$5.1\times(\pm2)10^5$	0.1	$6.0\ (\pm3)\times10^4$	0.2	$1.0(\pm1)\times10^2$
KD-4*	02IPE45	100	890	gl, ox, px, plg	–	0.3	$1.3\times(\pm1)10^5$	0.6	$3.8\times(\pm1)10^4$	2.2	$2.9(\pm1.4)\times10^3$
KD-5	KD-1	150	890		0.005	0.2	$5.4\times(\pm3)10^5$	0.3	$1.3\times(\pm0.7)10^4$	*tr*	$1.9(\pm0.2)\times10^4$
KD-6	KD-1	150	890		0.001	0.3	$2.4\times(\pm1)10^5$	1.3	$1.2\times(\pm0.4)10^5$	6.9	$1.5(\pm1)\times10^5$
KD-7	KD-1	150	890		0.0025	0.3	$4.4\times(\pm2)10^5$	0.5	$1.6\times(\pm0)10^4$	*tr*	$9.8(\pm2)\times10^2$
KD-8*	K-1R	75	900	gl, ox, px, plg (An_{39})	–	0.3	$5.0\times(\pm0.9)10^5$	0.8	$1.4\times(\pm1)10^5$	6.9	$6.3(\pm1)\times10^5$
KD-9*	K-19	75	875	gl, ox, px, plg (An_{36})	–	0.5	$3.2\times(\pm2)10^5$	0.9	$2.9\times(\pm1)10^5$	2.7	$1.2(\pm0.7)\times10^6$
KD-10*	02IPE45	100	890		–	0.2	$1.5\times(\pm1.5)10^5$	0.3	$1.9\times(\pm1)10^5$	0.5	$7.8(\pm5)\times10^4$
KD-11	KD-9	75	875		0.0025	2.3	$8.0\times(\pm4)10^5$	5	$1.5\times(\pm0.5)10^6$	11.8	$2.0(\pm0.7)\times10^6$
KD-12	KD-8	75	900		0.0025	0.4	$3.4\times(\pm1)10^5$	1.4	$3.7\times(\pm1)10^5$	2.7	$1.1(\pm0.6)\times10^6$
KD-13	KD-10	100	890		0.0025	0.3	$4.1\times(\pm0.9)10^5$	1	$2.9\times(\pm0.6)10^5$	3.9	$2.8(\pm1)\times10^5$
KD-14*	02IPE45	125	900	gl, ox, px	–	0.1	$1.4\times(\pm0.5)10^4$	*tr*	$5.2\times(\pm1)10^3$	0	0
KD-15	KD-10	100	890		0.001	0.2	$2.0\times(\pm0.7)10^5$	0.6	$2.1\ (\pm1)\times10^5$	6.7	$2.4(\pm1)\times10^5$
KD-16	KD-14	125	900		0.001	0.3	$5.0\times(\pm2)10^4$	0.2	$1.5\times(\pm1.5)10^4$	1	$2.0(\pm2)\times10^4$
KD-17*	02IPE45	100	890	gl, ox, px, plg	–	*tr*	$8.2\times(\pm2)10^4$	0.2	$7.3\times(\pm2)10^4$	0	0
KD-19	KD-17	100	890		0.01	0.7	$1.7\times(\pm0.7)10^5$	0.5	$3\times(\pm1)10^3$	13.4	$5.0(\pm5)\times10^2$
KD-20	KD-17	100	890		0.005	0.5	$1.3\times(\pm0.7)10^5$	0.8	$8\times(\pm4)10^3$	0.2	$3.5(\pm1.5)\times10^4$

KSU-23A were measured with a pycnometer, and those measurements were converted to bulk pumice densities, ρ_t. The vesicularity was then calculated using

$$Ves = \left(1-\frac{\rho_t}{\rho_g}\right) \tag{2}$$

by assuming a solid, vesicle-free density, ρ_g, of 2350 kg/m^3. The precision of this technique is estimated to be <0.03, based upon repeated measurements of the same sample.

Vesicle sizes and shapes were quantified through image analysis of back-scattered electron (BSE) images obtained with the electron microprobe. Thin sections of 15 randomly oriented 1–3 mm pumice from each of the Main and Gray phase fall samples KSU-23H and KSU-23A, and additional thin sections of larger pumice from Main and Gray phase units were used in these analyses. Enough pumice were imaged that, even with cut effects, the full range of vesicle shapes was measured. Most images were collected at 100× magnifications, although some images were collected at magnifications of 500–1500×. Grayscale images were converted to black and white images showing vesicles and solids. From those images, 3932 and 3088 vesicles were measured in white and gray pumice, respectively. The areas and dimensions of vesicles were then measured using ImageJ. Vesicle aspect ratios were calculated as the ratio of the long short axes, l and b, respectively. Equivalent vesicle radii, a, were calculated as:

$$a = \sqrt{lb}. \tag{3}$$

Capillary numbers of vesicles, Ca, were calculated using the relation of Hinch and Acrivos (1980):

$$\frac{l}{a} = 3.45\sqrt{Ca}. \tag{4}$$

Microlite textures of natural and experimental samples were quantified with analysis of BSE images. We define microlites in this study as crystals with the largest dimension smaller than 20 μm. Plagioclase, Fe–Ti oxide, pyroxene, and plagioclase microlites were outlined manually in each image and their sizes and area measured using ImageJ. Because of their similar appearance in BSE images, orthopyroxene and clinopyroxene were not differentiated, nor were ilmenite and titanomagnetite. Areal crystal number densities, N_A, were calculated using

$$N_A = \sqrt{\frac{n}{A}} \tag{5}$$

where n is the number of crystals of a particular phase counted in area A of glass only (Hammer et al., 1999). Three-dimensional number densities, N_V, were calculated from the two-dimensional measurements as

$$N_v = \sqrt{\frac{N_A^3}{\phi}} \tag{6}$$

where crystallinity, ϕ, is defined as the fraction of the vesicle-free image occupied by the microlite phase of interest.

For samples with three-dimensional microlite number densities of $\leq$1000 mm^{-3}, N_V was also measured directly using a petrographic microscope in transmitted light mode by counting the number of crystals in a known area and measuring the thickness of the sample. Because that technique counts crystals within a volume and does not extrapolate two-dimensional number densities into three-dimensional values, the technique has greater precision in measuring N_V at low number densities. This greater precision occurs because number densities calculated with the three-dimensional method are directly proportional to the number counted, whereas the values calculated with the two-dimensional technique are proportional to the number counted raised to the 3/2 power. Because the starting materials for decompression experiments contain microlites, number densities of decompression experiments were calculated as the difference of N_V measured in the decompression experiment and N_V of the experiment's starting material.

3. Results

3.1. Natural compositions

The KS_1 white and gray pumice are both rhyodacite, with 71.5–72.1 wt.% SiO_2, have nearly identical alkali concentrations (5.2–5.3 wt.% Na_2O and 1.4 wt.% K_2O), and differ by less than 0.1 wt.% in Al_2O_3 concentrations (Table 3; Izbekov et al., 2003). Trace element concentrations are similarly indistinguishable with, for example, 178–180 ppm Sr and 1.40–1.41 ppm Eu in both pumice. With few exceptions, the KS_1 white and gray pumice compositions differ by less than 5% (relative to each other).

Both white and gray pumice contain the same phenocryst assemblage: plagioclase, clinopyroxene, orthopyroxene, titanomagnetite, and ilmenite, in order of decreasing abundance. Plagioclase composes ~3 vol.% of the rock (vesicle-free) and occurs as 300–600 μm tabular crystals. Those crystals are optically clear, concentrically zoned, frequently twinned, and often host glass inclusions. Larger plagioclase phenocrysts often comprise a rounded core surrounded by a euhedral rim; although the zoning within such cores is generally concentric, it is rarely euhedral. Most plagioclase zones are An_{40}–An_{50} in composition, but can range from ~An_{35} to ~An_{60}. Rim compositions are An_{40}–An_{42}.

Clinopyroxene occurs generally as 200–400 μm prismatic phenocrysts and composes ~1 vol.% of the vesicle-free rocks. Those crystals are green and optically unzoned. Orthopyroxene is present in a similar abundance and occurs as 200–400 μm brown prisms. Occasional glass inclusions are hosted by pyroxene crystals, but less frequently than in plagioclase. Clinopyroxene is typically ~$En_{38}Fs_{21}Wo_{40}$, and orthopyroxene is typically ~$En_{56}Fs_{41}Wo_{28}$ (Table 3).

Titanomagnetite and ilmenite are the least abundant phenocryst phases and together compose <1 vol.%. Those two oxides occur as equant, euhedral crystals ~100 μm in size. Titanomagnetite and ilmenite crystals that are in contact are occasionally found. Titanomagnetite compositions are typically ~35 mol% ulvospinel; ilmenite phenocrysts range in composition from 76 to 85 mol% ilmenite (Table 3; Izbekov et al., 2003).

Matrix glass compositions of the two pumice types are also very similar (Table 3). All matrix glass is rhyolitic, with SiO_2 concentrations of 72.5(±0.9) wt.% and Na_2O concentrations of 5.4(±0.6) wt.%. Both pumice contain 2.7(±0.3) wt.% FeO and 2.3(±0.2) wt.% CaO.

Glass inclusions hosted by phenocrysts from white and gray pumice are compositionally indistinguishable and rhyodacitic in composition (Table 3). Although SiO_2 concentrations do not vary substantially between inclusions, water concentrations range from ~1.5 to 8 wt.%. Most of that range is likely a result of post-entrapment host crystallization and leaking during decompression and eruption (Supplemental material). No CO_2 was detected in the inclusions. Excluding inclusions with anomalously high and low water concentrations, the most reasonable pre-eruption water contents recorded by the inclusions are 4.4(±1.0) and 3.8(±0.9) wt.% H_2O for the white and gray pumice, respectively.

3.2. Natural vesicle and microlite textures

Both white and gray types of pumice have overlapping bulk vesicularities, 78.2±3.8 and 75.2±3.3 vol.%, respectively. Equivalent radii of vesicles in white and gray pumice are indistinguishable, 50 (±15) μm for both. Interestingly, however, the two pumice types have different vesicle shapes (Fig. 2). Vesicles in white pumice are more elongate: aspect ratios are typically >2:1 and can be >10:1 in white pumice, compared to vesicle aspect ratios <5:1 in gray pumice (Fig. 3).

More and larger microlites are present in gray pumice than in white (Fig. 2), resulting in much higher microlite crystallinity of the gray pumice, ~25%, than the white, <1%. Microlite number densities for plagioclase, pyroxene (clinopyroxene and orthopyroxene), and magnetite ± ilmenite are orders of magnitude higher in gray pumice. That difference is most apparent in plagioclase, where $2(\pm1)\times10^6$ mm^{-3} are present in gray pumice, whereas $1(\pm1)\times10^2$ mm^{-3} are present in white pumice. Pyroxene and Fe–Ti oxides are present in densities of ~4×10^6 mm^{-3} in gray pumice and 1–3×10^5 mm^{-3} in white pumice. Total microlite number densities are approximately ~4×10^5 and ~1.3×10^7 mm^{-3} for white and gray pumice, respectively. No fabrics are observed in microlite orientations in either white or gray pumice.

Size distributions of plagioclase microlites in gray pumice have modes of 2.0 μm, and are positively skewed (Fig. 4). In contrast, what few plagioclase microlites that are present in white pumice are all smaller than 2 μm. Pyroxene size distributions are coarser in gray pumice than in white, 2.0 μm compared to 1.0 μm, but have a similar skewness of 1.4–1.7 μm (Fig. 3). Iron–titanium oxides distributions in both pumice types have 1-μm modes and are positively skewed (Fig. 3).

3.3. Geothermometry of natural samples

Geothermometry of Fe–Ti oxide pairs were determined using the iron recalculation method of Stormer (1983) and the algorithm of

Table 3
Representative whole rock, glass, and mineral compositions of KS_1 white and gray pumice. Melt inclusions (*MI*) contain 3.8–4.4 wt.% H2O, whereas matrix glass (*MG*) is nearly anhydrous. Mineral analyses are presented for plagioclase (*plg*), clinopyroxene (*cpx*), orthopyroxene (*opx*), ilmenite (*ilm*), and titanomagnetite (*mt*). All analyses are given as weight percent oxides. Total iron is reported as FeO*. Uncertainties in matrix glass and melt inclusion microprobe analyses are indicated as (±1σ) for each element. Whole rock compositions were analyzed with XRF at Washington State University. Matrix glass, melt inclusions, and minerals were analyzed with electron microprobe.

Sample	SiO_2	Al_2O_3	TiO_2	FeO*	MnO	CaO	MgO	K_2O	Na_2O	Cr_2O_3	Total
White											
WR	71.48	14.54	0.449	3.14	0.142	2.84	0.78	1.37	5.18	–	100
MG	72.68	14.40	0.43	2.99	0.12	2.47	0.55	1.31	5.06	–	100
MI	73.39	13.13	0.27	2.5	0.14	1.67	0.14	1.24	3.22	–	100
plg	53.76	29.18	0.02	0.62	–	11.92	0.05	0.08	5.08	–	100.64
cpx	52.37	1.44	0.33	11.27	0.82	13.75	19.75	0.29	–	–	100.03
opx	52.79	0.62	0.18	23.91	1.86	19.39	1.35	0.03	–	–	100.12
ilm	–	0.17	45.48	49.04	1.22	–	2.48	–	–	0.04	98.43
mt	–	1.99	12.84	81.77	0.98	–	1.49	–	–	0.02	99.09
Gray											
WR	72.14	14.45	0.448	2.94	0.137	2.54	0.65	1.36	5.25	–	100
MG	73.54	13.38	0.38	2.88	0.15	2.48	0.6	1.29	5.29	–	100
MI	72.6	13.87	0.42	2.47	0.13	1.78	0.32	1.19	2.8	–	100
plg	54.94	28.37	0.04	0.55	–	11.08	0.03	0.06	5.23	–	100.3
cpx	52.71	1.05	0.24	12.69	1.11	13.95	18.43	0.28	–	–	100.47
opx	52.79	0.62	0.18	23.91	1.86	19.39	1.35	0.03	–	–	100.12
ilm	–	0.32	41.76	52.33	0.85	–	3.26	–	–	0.03	98.55
mt	–	1.99	12.33	81.54	0.95	–	1.55	–	–	0.06	100.58
Uncertainty	0.26	0.17	0.05	0.15	0.04	0.05	0.02	0.1	0.16	–	

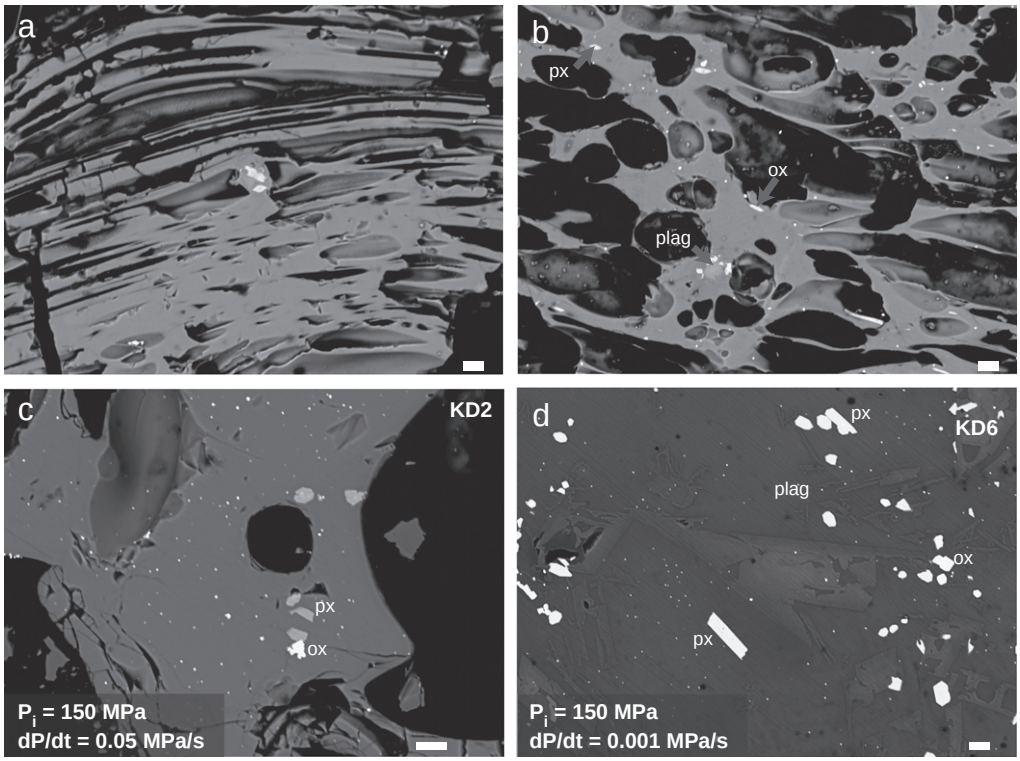

Fig. 2. Representative textures of KS_1 pumice and decompression experiments. a) White pumice (a) are composed of microlite-free glass. Vesicles in white pumice are commonly elongate and have aspect ratios >10:1. In contrast, gray pumice (b) contain abundant oxide (ox), pyroxene (px), and plagioclase (plag) microlites. Vesicles in gray pumice are generally round with aspect ratios <3:1. In experiments KD-2 (c) and KD-6 (d), decompressed from initial pressures Pi = 150 MPa, microlite number density and size increase as decompression rate slows from 0.05 to 0.001 MPa s^{-1}, such that although no plagioclase microlites are present in KD-2, abundant swallow-tail and skeletal plagioclase microlites are present in KD-6. The white scale bars in all images are 10 μm.

Anderson and Lindsley (1988). Temperature estimates were limited to touching pairs of titanomagnetite and ilmenite phenocrysts; Mg and Mn contents of those pairs indicate that they are in equilibrium (Bacon and Hirschmann, 1988). In addition, application of the program QUILF to electron microprobe analyses of Fe–Ti oxides, clinopyroxene, and orthopyroxene indicates equilibrium between all Fe–Ti–Mg phases (Anderson et al., 1993). Analyses of 12 oxide pairs from white pumice and 8 pairs from gray pumice indicate overlapping temperatures of 891 ± 8 °C for the white and 897 ± 6 °C for the gray pumice (Bindeman et al., 2010). Consideration of white and gray oxide pairs together yields equilibrium temperatures of 895 ± 5 °C. Those analyses also indicate oxygen fugacities of ~$10^{-11.5}$ bars, or approximately $\log(f_{O2}) = \mathrm{NNO} + 1$.

3.3.1. Experimental phase equilibria

At all pressures and temperatures examined, silicate melt (glass) and Fe–Ti oxides are stable (Fig. 5). We did not distinguish between titanomagnetite and ilmenite. As expected, both plagioclase and pyroxene are stable as water pressure and/or temperature decreases. For example, at 200 MPa, plagioclase and pyroxene are stable only below 825 °C and 875 °C, respectively, whereas at 100 MPa they are both stable above 900 °C.

Plagioclase varies systematically in composition with temperature and pressure (Fig. 5). For example, at 100 MPa, anorthite content of plagioclase increases from An_{30} to An_{43} as temperature increases from 800 to 900 °C. Anorthite content increases by ~5 mol% *An* over a pressure range of ~50 MPa: at 850 °C plagioclase of composition An_{30} and An_{35} is stable at 50 and 100 MPa, respectively.

Glass compositions vary systematically with temperature (Supplemental material). Iron and calcium concentrations increase with temperature: at 100 MPa, FeO increases linearly from 1.5 wt.% to 2.75 wt.% and CaO increases from 1.25 to 2.4 wt.% as temperature increases from 800 to 925 °C. Silica concentration decreases with increasing temperature: in samples run at 100 MPa, silica concentration decreases from 75 wt.% to 69 wt.% as temperature increases from 800 to 925 °C. Variation of glass compositions with pressure is less dramatic. In general, iron and calcium concentrations increase by ~0.5 wt.% as pressure increases from 100 to 200 MPa. Silica concentration decreases by 1–2 wt.% as pressure increases from 100 to 200 MPa.

3.4. Decompression experiments

3.4.1. Decompression from 150 MPa at 890 °C

Five experiments were decompressed from 150 MPa at 890 °C (Fig. 6). The starting material for those experiments contained no plagioclase, $1.3(\pm 0.5)\times 10^3$ mm^{-3} pyroxene, and $3.6(\pm 2)\times 10^4$ mm^{-3} Fe–Ti oxide microlites. Experiments decompressed at 0.05 MPa s^{-1} nucleate no plagioclase. As decompression rate decreases from 0.01 to 0.001 MPa s^{-1}, plagioclase density increases from $1.0\ (\pm 1)\times 10^2$ to $1.5\ (\pm 1)\times 10^5$ mm^{-3}. Pyroxene number densities do not vary substantially with decompression rate and are 10^4 to 10^5 mm^{-3}. The number densities of Fe–Ti oxides decrease from $1.0(\pm 0.5)\times 10^6$ mm^{-3} at 0.05 MPa s^{-1} to $1.3(\pm 0.4)\times 10^5$ mm^{-3} at 0.001 MPa s^{-1}.

The mode of plagioclase microlite size is 2–4 μm in all experiments where present, but the distribution of sizes becomes more positively skewed as decompression rate decreases (Fig. 4). Pyroxene size distributions, on the other hand, are affected more complexly by decompression rate (Fig. 4). As decompression rate decreases from 0.05 to 0.005 MPa s^{-1}, the mode coarsens from 1–2 to 4–6 μm and skewness increases from 0.7 to 1 μm. As decompression rate is further reduced, to 0.005 MPa s^{-1}, the mode decreases to 3.5 μm and skewness increases to 1.6 μm. At decompression rates of 0.0025 and 0.001 MPa s^{-1}, the mode is <2 μm and skewness decreases to <0.5 μm. Over the range in decompression rates, the mode in Fe–Ti oxide microlite size remains ~1 μm, but skewness of the distributions decreases systematically from 5.5 μm at 0.05 MPa s^{-1} to 1.4 μm at 0.001 MPa s^{-1} (Fig. 4).

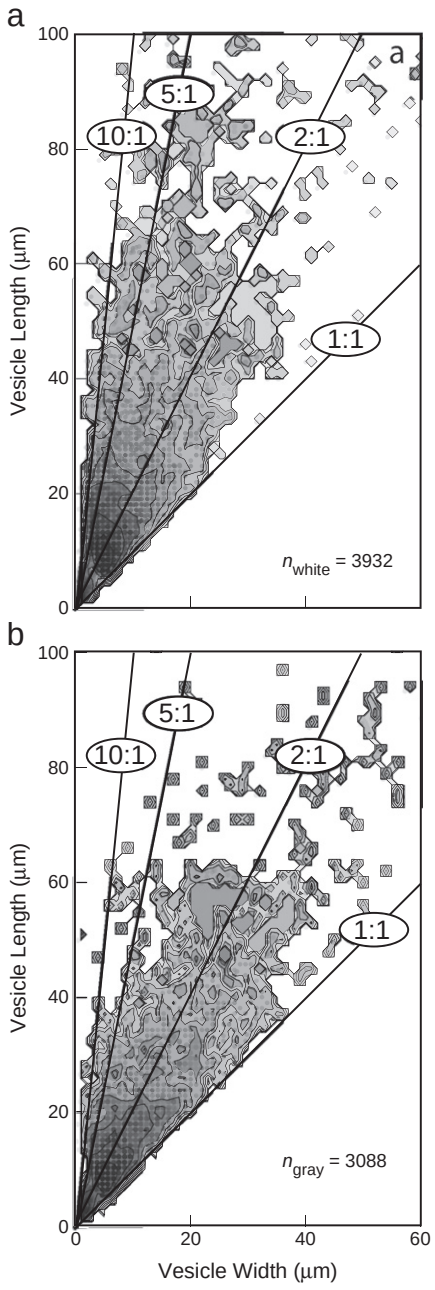

Fig. 3. Vesicle sizes in white and gray pumice. Vesicles in white pumice (a) are typically more elongate than those in gray pumice (b). Although the two populations overlap, most vesicles in white pumice have aspect ratios (long:short) greater than 2:1 (and as high as ~20:1), whereas most vesicles in gray pumice have aspect ratios less than 5:1. Aspect ratios of vesicles are indicated by diagonal lines extending from the origin, e.g., 2:1.

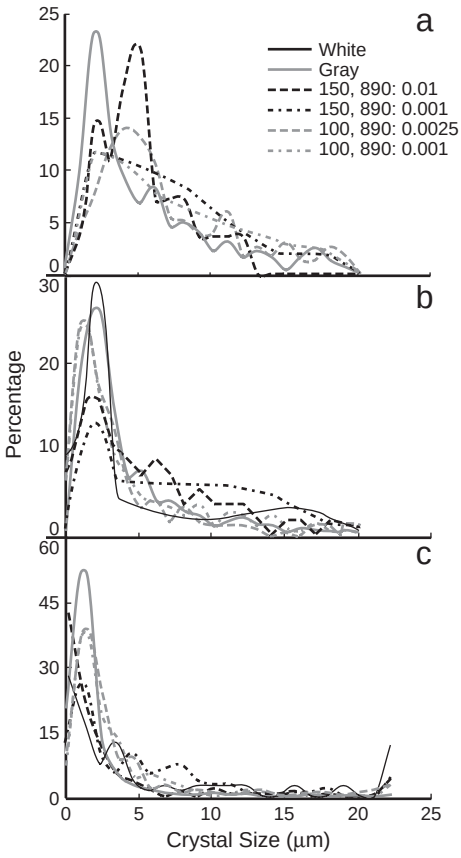

Fig. 4. Microlite size distributions of natural pumice and representative decompression experiments. a) Plagioclase microlites are nearly absent in white pumice, whereas gray pumice have unimodal CSDs with a mode at ~2 μm. In decompression experiments, plagioclase microlites have unimodal distributions that coarsen and develop tails as initial pressure and decompression rate decrease. b) Pyroxene microlites have unimodal distributions with prominent modes at 2 μm. As initial pressure decreases, those modes become more prominent. c) Oxide microlites in experimental samples have unimodal distributions with most crystals smaller than 2 μm. As decompression rate and initial pressure decrease, skew of the distributions increases. All data are shown as count percentages binned in 2-μm intervals. Size distributions of experiments decompressed from 75 MPa or at 0.005 MPa s^{-1} are not plotted in order to keep the plots uncluttered.

3.4.2. Decompression from 100 MPa at 890 °C

Four experiments were decompressed from 100 MPa at 890 °C (Fig. 6). The initial material for those experiments contained 7.8 $(\pm 5)\times 10^4$ mm^{-3} plagioclase, 1.9$(\pm 1)\times 10^5$ mm^{-3} pyroxene, and 1.5 $(\pm 1.5)\times 10^5$ mm^{-3} Fe–Ti oxide microlites. Plagioclase number density increases from 5$(\pm 5)\times 10^2$ to 2.4$(\pm 1)\times 10^5$ mm^{-3} as decompression rate decreases from 0.01 to 0.001 MPa s^{-1}. Pyroxene number density increases from 3$(\pm 1)\times 10^3$ to 2.9$(\pm 0.6)\times 10^5$ mm^{-3} as decompression rate decreases. Similarly, Fe–Ti oxide number densities increase from 1.3$(\pm 0.5)\times 10^5$ to 4.1$(\pm 0.7)\times 10^5$.

The modes of plagioclase size distributions increase from 1–2 to 4–6 μm as decompression rate decreases (Fig. 4). Skewness of those distributions decreases from 1.0 to 0.6 μm. The mode of pyroxene microlite sizes increases from 1 μm at 0.01 MPa s^{-1} to 3 μm at 0.005 MPa s^{-1}, but as decompression decreases further, the skewness increases from 0.6 to >1.4 μm, and the mode returns to 1 μm (Fig. 4). Skewness of Fe–Ti oxide size distributions decreases systematically from 3.7 to 2.3 μm as decompression rate slows from 0.01 to 0.001 MPa s^{-1}, but the modes of those distributions remain ~1 μm (Fig. 4).

3.4.3. Decompression from 125 MPa at 900 °C

One experiment was decompressed from 125 MPa at 900 °C (Fig. 6). The initial material for that experiment contained no plagioclase, 5.2 $(\pm 1.0)\times 10^3$ mm^{-3} pyroxene, and 1.4$(\pm 0.5)\times 10^4$ mm^{-3} Fe–Ti oxides. The experiment decompressed at 0.001 MPa s^{-1} contains 0–4$\times 10^4$ mm^{-3} plagioclase and 0–3$\times 10^4$ mm^{-3} pyroxene. The number density of Fe–Ti oxides is the lowest measured in any experiment, 3–7$\times 10^4$ mm^{-3} (Fig. 4). The size distributions of plagioclase and pyroxene microlites are very broad and have no recognizable modes. The size distribution of Fe–Ti oxide microlites has a mode of 1 μm, skewness of 2.3, and is similar in appearance to experiments decompressed at 0.0025 MPa s^{-1} from 150 MPa and 890 °C.

3.4.4. Decompression from 75 MPa

Two experiments were decompressed at 0.0025 MPa s^{-1} from 75 MPa at temperatures of 875 and 900 °C (Fig. 4). The starting materials

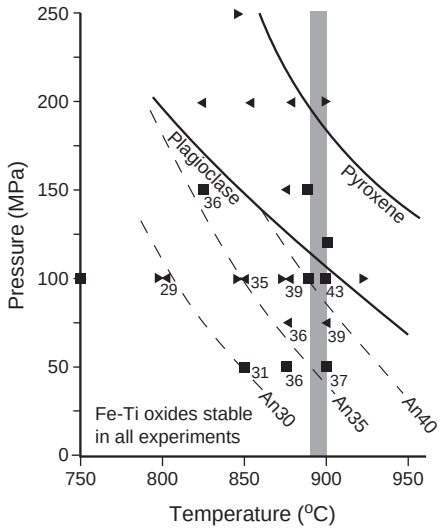

Fig. 5. KS_1 phase equilibria. The phase assemblage of Fe–Ti oxides, clinopyroxene, orthopyroxene, and plagioclase ($\sim An_{42}$) is stable at conditions of 100–125 MPa and ~895 °C. Fe–Ti oxide equilibrium temperatures of 895 ± 5 °C are indicated by the shaded box. Right and left pointing triangles indicate melting and crystallization experiments, respectively. Anorthite contents of plagioclase in crystallization and "straight-in" experiments are labeled; dashed lines contour those data and indicate anorthite content. Experiments are listed in Table 2.

for those experiments contained $1.2(\pm 0.7)\times 10^6$ mm^{-3} plagioclase, $2.9(\pm 1.0)\times 10^5$ mm^{-3} pyroxene, and $3(\pm 2)\times 10^5$ mm^{-3} Fe–Ti oxide microlites at 875 °C, and $6.3(\pm 1.0)\times 10^5$ mm^{-3} plagioclase, $1.4(\pm 1.0)\times 10^5$ mm^{-3} pyroxene, and $5.0(\pm 0.9)\times 10^5$ mm^{-3} Fe–Ti oxide microlites at 900 °C. The 875 °C experiment contains more plagioclase microlites than does the 900 °C experiment: $2.0(\pm 0.7)\times 10^6$ compared to $1.1(\pm 0.6)\times 10^6$ mm^{-3} (Fig. 4). Pyroxene microlite number densities decrease from $1.5(\pm 0.5)\times 10^6$ mm^{-3} at 875 °C to $4(\pm 1)\times 10^5$ mm^{-3} at 900 °C (Fig. 4). Fe–Ti oxides show a similar pattern, decreasing from densities of $8(\pm 4)\times 10^5$ to $3.4(\pm 1.0)\times 10^5$ mm^{-3} as temperature increases (Fig. 4). The modes of plagioclase size increases from 1.8 to 2.4 μm as temperature increases from 875 to 900 °C, and skewness decreases from 1.3 to 1.0 μm. In contrast, pyroxene modes decrease from 4.0 to 1.9 μm and skewness increases from 1.4 to 2.4 μm. Fe–Ti oxide size distribution modes decrease from 2.7 to 1.9 μm and skewness increases from 0.9 to 1.0 μm.

3.4.5. Compositions of decompression experiments

Glass compositions vary systematically with starting conditions and decompression rates, particularly for rates lower than 0.01 MPa/s (Fig. 7). For experiments decompressed from 100 MPa or greater pressure, initial SiO_2 concentration is 73–73.5 wt.%. In the 100 MPa set of experiments, the SiO_2 concentration increases to >75 wt.% as decompression rate decreases to <0.001 MPa/s. In the 150 MPa experiments, SiO_2 concentration remains relatively constant until decompression rate falls below 0.0025 MPa/s and SiO_2 increases to >74 wt.%. The concentration of Al_2O_3 remains effectively constant in most experiments until decompression rate falls below 0.005 MPa/s, and Al_2O_3 concentration decreases by 0.1 to 0.5 wt.% in the 100, 125, and 150 MPa runs. In the 150 MPa set of experiments, CaO decreases from ~2.45 to 2.3 wt.% as decompression slows to 0.0025 MPa/s, and then rapidly decreases to 1.7 wt.% as decompression rate falls to 0.001 MPa/s, whereas CaO concentration smoothly decreases from ~2 wt.% to <1.5 wt.% with decreasing decompression rate in the 100 MPa experiments. Titanium decreases with reduced decompression rate in the 150 and 125 MPa decompression runs, from >0.4 wt.% initial concentration to ~0.37 wt.% in 0.001 MPa/s experiments, but remains relatively constant in experiments decompressed from lower pressures.

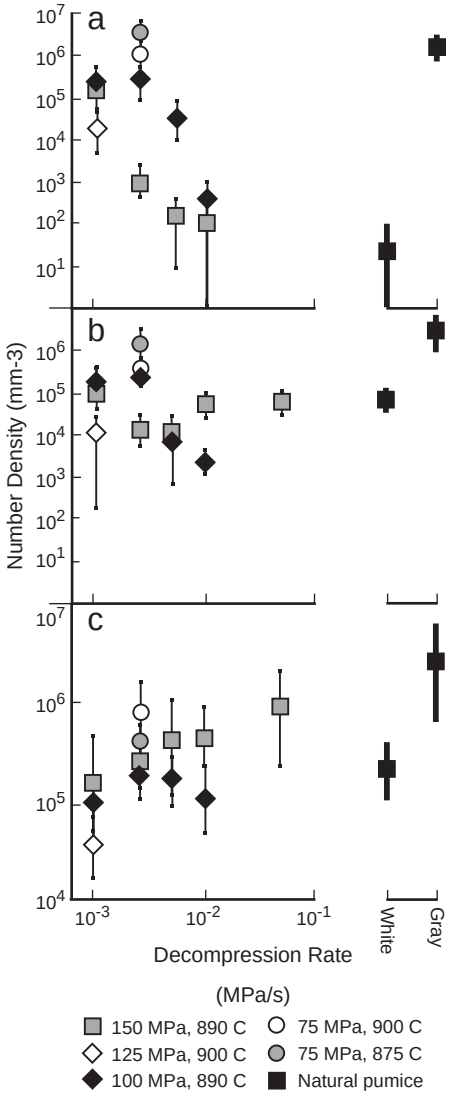

Fig. 6. Variation in microlite N_V with decompression rate. a) Volumetric number densities of plagioclase increase with decreasing decompression rate. Experiments run at lower temperatures or initial pressures have higher plagioclase number densities. b) Volumetric number densities of pyroxene increase with decreasing decompression rate for experiments decompressed from 100 MPa, but are relatively constant in experiments initiated from 150 MPa. c) Oxide number densities decrease with decreased decompression rate in experiments initiated from 150 MPa, but do not change significantly in experiments decompressed from 100 MPa. Error bars are one standard deviation.

4. Discussion

4.1. Eruption of one magma during the KS_1 eruption

Many eruptions tap multiple magmas (Hildreth, 1983; Pallister et al., 1996; Hammer et al., 1999). Often those compositional differences give rise to color contrasts and provide a means of recognizing different magma types in the field. Following that line of reasoning, the KS_1 white and gray pumice could be easily interpreted as originating from two different magmas. That interpretation is however, wrong, as several lines of evidence indicate a single magma erupted to produce the KS_1 white and gray pumice. First, bulk compositions of the white and gray pumice are indistinguishable. Second, phase assemblages and phenocryst and matrix glass compositions are effectively the same. Compositions of coexisting minerals indicate that both the white and gray pumice originated from the same magma with the same pressure, temperature, and oxygen fugacity. Third, glass inclusions from white

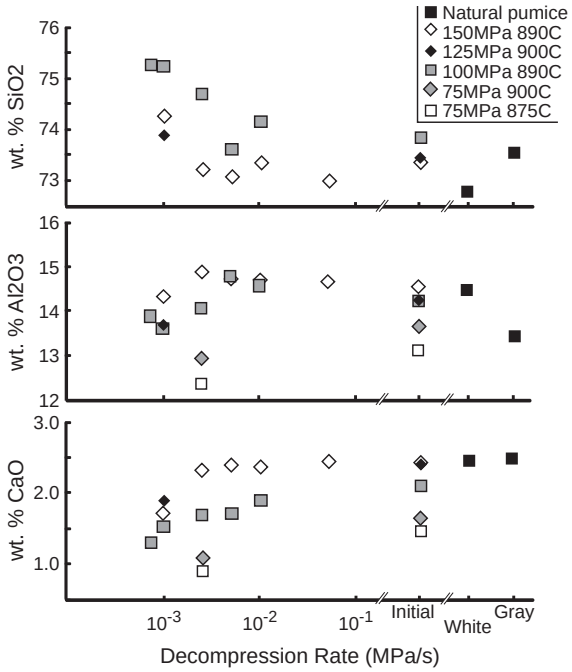

Fig. 7. Glass compositions of decompression experiments and natural pumice. a) SiO_2 compositions decrease with increased decompression rate, initial pressure, and temperature. Experiments decompressed from 75 MPa are not shown as they exceeded 75.5 wt.% SiO_2. b) Al_2O_3 concentration remains relatively steady in experiments decompressed from 150 MPa until the decompression rate falls below 0.0025 MPa/s. In experiments decompressed from 100 MPa, the concentration drops as the rate decreases below 0.005 MPa/s. c) Calcium concentrations remain stable in 150 MPa experiments until the decompression rate decreases below 0.0025 MPa/s, whereas they systematically decrease as decompression rate falls in runs decompressed from 100 MPa.

and gray pumice contain overlapping water concentrations and, using the model of Moore et al. (1998), indicate saturation pressures of 110–150 MPa. Assuming a temperature of 895 °C from geothermometry (Izbekov et al., 2003; Bindeman et al., 2010), we find that the natural phase assemblage is stable at pressures less than 125 MPa, where plagioclase stability begins (Fig. 5). Compositions of plagioclase rims from experiments run at 100 MPa and 900 °C are most consistent with the compositions of natural samples, further constraining storage conditions of the rhyodacite (Fig. 5). At pressures of 100 MPa, experimental glass compositions become more siliceous and less calcic than natural matrix glass as temperature drops below 875 °C (Supplemental material). It is highly unlikely that two magmas of the same composition and stored at the same conditions existed simultaneously and in isolation from one another beneath the Ksudach edifice prior to the KS_1 eruption. Instead, the most reasonable explanation is that the white and gray pumice originated from a single magma stored at 110–125 MPa, equivalent to a depth of 4–5 km, and 895(±5)°C. That pressure is consistent with dissolved water contents of 4.4(±1.0) and 3.8(±0.9) wt.% for the white and gray pumice.

4.2. Decompression rates of KS_1 pumice

Given that the only differences between the white and gray pumice are textural, and the two pumice types are aliquots of the same magma, we suggest that those differences result from different decompression and ascent rates during the eruption. That the gray pumice contain more microlites indicates it decompressed slower than the white pumice. Our decompression experiments provide a quantitative estimate for decompression rates of the white and gray pumice. It should be noted here that although we only investigated one type of decompression (i.e., multi-step decompressions defining a constant decompression rate), several arguments suggest our decompression experiments are applicable to the Ksudach system. First, the multiple decompression steps in our experiments should more closely simulate the natural system than single-step decompressions (i.e., decompressing to the final pressure and then holding for a designated interval before quenching); although each decompression step disturbs the system, and may create a nucleation event, the magnitude of each disturbance (which increases plagioclase undercooling by ~6.5 °C) is quite small. Second, Browne and Gardner (2006) demonstrated that hornblende reaction rates are greatly dependent on the amount spent at specific disequilibrium pressure–temperature conditions, not just the average decompression rate, thus single-step decompressions (i.e., decompression accomplished in a single decrease followed by maintenance of the final pressure for a length of time appropriate for the desired average decompression rate) can fail to produce textures observed in multi-step decompressions and natural samples; it seems reasonable that similar processes should apply to plagioclase, pyroxene, and oxide crystallization kinetics. Lastly, although magma decompression rate increases during ascent, numerical modeling of ascent suggests that most of the acceleration occurs during the final ~10% of the total decompression time (Mastin and Ghiorso, 2000; Mastin, 2002), thus constant rate decompression experiments should provide a reasonable model of actual magmatic decompression and ascent.

White pumice are characterized by plagioclase number densities $<5\times10^2$ mm^{-3} and pyroxene and Fe–Ti oxide densities of 1–4×10^5 mm^{-3}. Plagioclase number densities of experiments decompressed from 150 or 100 MPa at rates equal to or greater than 0.01 MPa s^{-1} correspond well with the natural samples; all experiments decompressed at slower rates produce plagioclase densities that far exceed those of white pumice. Number densities of pyroxene microlites in experiments decompressed from 150 MPa are all less than the natural samples, but experiments decompressed slower than 0.005 MPa s^{-1} from 100 MPa reproduce the values found in white pumice. Pyroxene are less abundant in the experiment decompressed at 0.001 MPa from 125 MPa, whereas the experiments decompressed at 0.0025 MPa from 75 MPa both contain more pyroxene than do natural samples. Fe–Ti oxide number densities of all decompression experiments, except that initiated at 125 MPa, are in agreement with the natural value.

Pyroxene microlite size distributions within white pumice are positively skewed and have a mode of 2 μm, Fe–Ti oxide distributions are unimodal with most crystals <2 μm and no crystals larger than 8 μm; insufficient plagioclase are present for reliable size distributions. Experiments decompressed from 150 MPa have either the appropriate mode (at 0.01 MPa s^{-1}) or skewness (at 0.005 MPa s^{-1}) but not both. In contrast, the sample decompressed at 0.001 MPa s^{-1} from 100 MPa reproduces both the mode and skewness of the size distribution. Fe–Ti oxide size distributions of all experiments except those decompressed from 75 MPa are more positively skewed than the natural samples, but the modes of all experiments except those decompressed from 75 MPa compare are similar to the natural samples.

Matrix glass compositions of the white pumice are most consistent with experiments decompressed from ≥125 MPa at >0.0025 MPa/s, or from 100 MPa at >0.01 MPa/s. Experiments decompressed from either lower initial pressures or at slower rates have excess SiO_2, >74 wt.%, and insufficient Al_2O_3 and CaO, <14.5 and <2 wt.%, respectively, in comparison with natural samples. Because little compositional variation is present between experiments decompressed at faster rates, glass composition does not constrain the maximum decompression rate of the white pumice.

In gray pumice, plagioclase microlites are present in densities of ~2×10^6 mm^{-3}, and pyroxene and Fe–Ti oxide microlites occur in densities of ~5–6×10^6 mm^{-3}. Experiments decompressed at 0.0025 MPa s^{-1} from 100 MPa have plagioclase abundances that approach the natural number densities, as do experiments decompressed from 75 MPa; all other experiments contain fewer plagioclase than the natural samples. The only experiment containing pyroxene in densities

comparable to gray pumice is the sample decompressed at 0.0025 MPa s^{-1} from 75 MPa at 875 °C. Fe–Ti oxide number densities of all but the slowest (0.001 MPa s^{-1}) experiment decompressed from 150 MPa correspond well with those of the gray pumice, as do experiments decompressed at 0.0025 MPa s^{-1} from 100 to 75 MPa.

Size distributions of plagioclase and pyroxene microlites in gray pumice have 2-μm modes and skewness of 1.2 and 1.7 μm. Fe–Ti oxide distributions have modes of 1 μm and no microlites coarser than 6 μm. Plagioclase size distributions of the experiment decompressed at 0.001 MPa s^{-1} from 100 MPa reproduce the mode of the natural size distribution, but contain more crystals in the coarse tail, whereas the experiment decompressed at 0.0025 MPa s^{-1} from 100 MPa reproduces the coarse tail of the natural samples but has a mode that is too coarse; the experiment decompressed at 0.0025 MPa s^{-1} from 75 MPa at 875 °C nearly matches the natural distribution. Samples decompressed at ≤0.0025 MPa s^{-1} from 100 MPa and 890 °C have pyroxene size distributions that fit the natural samples. The experiment decompressed at 0.0025 MPa s^{-1} from 75 MPa and 900 °C also reproduces the gray pyroxene size distributions. Fe–Ti oxide size distributions of experiments decompressed at 0.0025–0.005 MPa s^{-1} from 150 and 100 MPa correspond well with the natural size distributions; the experiment decompressed at 0.001 MPa from 125 MPa and 900 °C also reproduces the natural distribution. Experiments decompressed at slower rates or from lower initial pressures contain Fe–Ti oxide size distributions that are either less positively skewed or coarser than the natural distributions.

Matrix glass compositions of the gray pumice are similar to experiments decompressed from >100 MPa at rates of 0.001–0.0025 MPa/s. The natural SiO_2 and CaO concentrations, 73.5 and 2.5 wt. %, respectively, are consistent with experiments decompressed at ≥0.0025 MPa/s, whereas the Al_2O_3 concentration, 13.4 wt.%, suggests decompression at 0.001 MPa/s. Experiments decompressed at slower rates contain too much SiO_2 and too little CaO, and faster rate experiments contain too much Al_2O_3.

Based on results of decompression experiments and pre-eruptive storage conditions of 895 °C and 110–125 MPa, the most reasonable decompression rate for the white pumice is ≥0.01 but less than 0.1 MPa s^{-1}, corresponding to total decompression times of <3 h. Experiments decompressed at those rates reproduce plagioclase number densities and matrix glass compositions in agreement with white pumice. Fe–Ti oxide number densities also support those decompression rates. Decompression experiments and pre-eruptive storage conditions indicate gray pumice most likely decompressed at 0.0025 MPa s^{-1}, corresponding to a total decompression time of 8–11 h. Experiments decompressed at that rate from 100 MPa reproduce gray pumice plagioclase number densities and sizes, pyroxene sizes, Fe–Ti oxide number densities and sizes, and matrix glass compositions. Insufficient plagioclase densities are present at faster decompression rates, and slower rates fail to produce the observed microlite size distributions.

4.3. Changes in ascent rate coincident with caldera collapse

The change from white to gray pumice occurred immediately after the Lithic phase, when caldera collapse is thought to have begun (Andrews et al., 2007). Thus the reduction in magma decompression rate occurred immediately after caldera formation began. That timing poses two important and related questions: why did decompression rate decrease, and why was that decrease coincident with caldera collapse?

Change in either the driving pressure or conduit dimensions could result in a reduced decompression rate. We assume that decompression occurs primarily in the conduit during ascent, and that decompression in the chamber at depth is insignificant. That assumption is valid for several reasons. The magnitude of the change in decompression rate and its timing strongly argue against reduction in chamber pressure as the sole cause of slowed ascent. Notably, Druitt and Sparks (1984) suggested that caldera formation occurs when chamber overpressure is relieved and the edifice collapses. Although we do not rule out pre-eruptive overpressure of the KS_1 magma chamber, bleeding off the maximum possible overpressure that crustal rocks can sustain, <25 MPa (Druitt and Sparks, 1984; Roche and Druitt, 2001), would result in a maximum reduction in decompression rate of ~25% (e.g., 0.01 MPa s^{-1} reducing to 0.0075 MPa s^{-1}); significantly less than the observed ~75% decrease (0.01 MPa s^{-1} to 0.0025 MPa s^{-1}). In addition, if the pressure in the chamber decreased by the ~75% necessary to reduce the decompression rate by a factor of 4 and the conduit geometry did not change, then the mass flux would also decrease by a factor of 4, conflicting with the observed relatively stable mass flux. Moreover, the Druitt and Sparks model predicts that collapse should occur relatively early, not after ~2/3 of the magma has erupted. If a reduction in chamber overpressure during early stages of eruption is responsible for the reduced decompression rate during the Gray phase, then the decompression rate should have progressively decreased through the Initial, Main, and Lithic phases as the chamber partially emptied and overpressure waned; white pumice textures show no evidence of decreased decompression rate between Initial, Main, and Lithic phases. Further, had significant *in situ* decompression occurred, then it should have continued through the 24-hour duration of the Gray phase resulting in textural differences between early- and late-erupted Gray phase pumice; no such changes are observed. Lastly, the mass fluxes of the various eruption phases provide insight to eruption duration and argue against gradual, *in situ* decompression prior to and during eruption of the Gray phase. Specifically, the total time required to produce the observed textures in gray pumice is ~8–11 h, which is substantially less than the >32 h that elapsed between the start of the eruption and the onset of erupting gray pumice. As a result, gradual decompression of the chamber at depth during the course of the eruption cannot explain the increased microlite content or sudden appearance of the gray pumice.

By assuming that decompression occurs primarily during ascent, ascent velocity is the ratio of decompression rate to the lithostatic pressure gradient

$$u = \frac{\frac{dP}{dt}}{\frac{dP}{dz}}. \tag{7}$$

The reduced decompression rate recorded by Gray phase groundmass textures thus reflects a ~75% reduction in ascent velocity. Assuming a lithostatic pressure gradient of 25 MPa/km, the average white and gray decompression rates correspond to ascent rates of >0.4 and 0.1 m/s, respectively.

Vesicle textures record strain in the magma during decompression and ascent and support a reduced ascent rate during the Gray phase. The capillary number, Ca, provides a means of estimating shear rates through the equation:

$$Ca = \frac{aG\mu}{\Gamma} \tag{8}$$

where G is shear rate, m is melt viscosity, and Γ is surface tension (e.g., Rust and Manga, 2002). Because the white and gray pumice formed from the same magma, viscosity and surface tension may be treated as equals in comparison of the two vesicle populations. Thus variation in the capillary number between the two pumice types is the result of changes in either equivalent vesicle radius or shear rate. As the equivalent radius is known for each vesicle, the relative shear rates recorded by each vesicle may be estimated.

Assuming surface tension of 0.15 N m^{-1} (from extrapolation of the hydrous rhyolite data presented by Mangan and Sisson, 2005) and viscosity of ~10^5 Pa s calculated using the methods of Spera (2000), the average shear rates recorded by all measured vesicles are ~4.3×10^{-7} s^{-1}

and ~2.9×10^{-7} s^{-1} in the white and gray pumice, respectively. If only the 5% of vesicles with the largest capillary numbers are considered, the white pumice record ~50% higher shear rates than the gray, $2.8(\pm1)\times10^{-6}$ s^{-1} compared to $1.8(\pm1)\times10^{-6}$ s^{-1}. Those higher shear rates are consistent with faster ascent of the white pumice compared to the gray pumice.

4.4. Changes in conduit geometry coincident with caldera collapse

A simple estimation of conduit size, A, can be made from mass flux using

$$A = \frac{\frac{dM}{dt}}{\rho u} \tag{8}$$

where dM/dt is the eruptive mass flux, ρ is magma density, and u is average ascent velocity (from Eq. 7). Comparison of mass fluxes and ascent velocities of the Main and Gray phases indicate that the conduit size increased by a factor of ~4 following the initiation of caldera collapse. Such a relation is, however, a simplification and ignores the dependence of ascent rate on conduit size and shape (Jaupart, 2000; Mastin and Ghiorso, 2000; Mastin, 2002).

Numerical models offer a more sophisticated method of balancing conduit size, mass flux, and decompression rate (Mastin and Ghiorso, 2000; Mastin, 2002). Specifically, the program Conflow allows us to examine the effects of conduit geometry on mass flux and decompression rate, and thus estimate conduit geometries of the Main and Gray phases by comparing model runs with estimated mass fluxes and experimental decompression rates. For our simulations, we calculated the average decompression rate from

$$\frac{dP}{dt} = \frac{\Delta P}{\sum \frac{z_i - z_{i-1}}{u_i}} \tag{9}$$

where ΔP and z_i are the total pressure drop and distance ascended through step i, and u_i is the velocity of that step. The average decompression rate of any given model run is taken as the average dP/dt (Eq. 9) calculated from the base of the conduit up to when the model flow reaches a vesicularity of 70% (the fragmentation point in Conflow). We should note that if taken as exact predictors of conduit geometry, Conflow solutions are often implausible, the model does, however, provide outer bounds for and constrain critical aspects of conduit geometry. For example, model-predictions of a straight-sided cone may be geologically accommodated by a generally broad conduit with a constricted upper region. Although the Conflow solutions to the KS_1 eruptive mass fluxes and decompression rates are not unique, they do provide important insight to syn-eruptive changes in conduit structure.

The mass flux of the Main phase can be modeled by a single cylindrical conduit with a diameter of 120–150 m. The decompression rate within that conduit is 0.30 MPa s^{-1} to 0.35 MPa s^{-1}. Both of those rates are significantly higher than the estimated minimum decompression rate for white pumice, 0.01 MPa s^{-1}. If we attempt to solve for decompression rate, we model decompression rates of 0.01 MPa s^{-1} if conduit diameter is 20 m. Such a size, however, results in a mass flux more than 2 orders of magnitude below that of the Main phase.

If we consider non-cylindrical conduits, then a single, tapering conduit can simultaneously accommodate the required mass flux and approach the minimum decompression rate estimated for the Main phase. Modeling indicates that a single conical (or constricted) conduit with a basal diameter of ~400 m and a vent diameter of 100 m can accommodate a mass flux of ~4×10^{8} kg s^{-1} with a decompression rate of ~0.05 MPa s^{-1}. If the conduit base is broadened to 1000 m, and the vent is constricted to 75 m, mass flux remains >3×10^{8} kg s^{-1}, and decompression rate slows to ~0.01 MPa s^{-1}. More conical geometries fail to predict the required mass flux and/or predict decompression rates that are too low.

The Gray phase mass flux can be modeled by a single cylindrical conduit with a diameter of 100–130 m. The decompression rate within such a conduit, ~0.2 MPa s^{-1}, however, is two orders of magnitude greater than that estimated from decompression experiments, 0.0025 MPa s^{-1}. It is thus unlikely that a single cylindrical conduit fed the Gray phase. Cylindrical conduits with diameters <20 m predict decompression rates approaching those of the Gray phase, but the mass fluxes through those conduits are two orders of magnitude too low.

The presence of multiple, cylindrical conduits during the Gray phase is one way to solve simultaneously for mass flux and decompression rate, but this solution seems unlikely for several reasons. First, the Gray phase mass flux requires approximately 100 conduits with 20-m diameters to operate simultaneously during the eruption phase. Such a large number is unreasonable because those conduits would have to be near enough to one another that they all fed the same Plinian column, but far enough apart that they did not coalesce, as coalescence would result in a larger conduit and an increase in decompression rate. Furthermore, it is unlikely that such a large number of conduits could remain active for the duration of the Gray phase without conduit heterogeneities leading to the widening of some conduits and increases in decompression rate. Similarly, were all of those conduits to coalesce into a ring-dike, it is hard to imagine that dike maintaining a uniform aperture throughout the Gray phase, and far more likely that magma ascent would become focused along certain segments, leading to changes in mass flux and/or decompression rate.

A single conduit can model the Gray phase mass flux and decompression rate if it has a conical or constricted geometry. A conical conduit that tapers from 1200 to 1600 m at its base to a vent of ~60 m can simultaneously accommodate the required mass flux and decompression rate. If mass flux is evenly distributed among two, three, or four conduits, those conduits still require basal diameters of ~1000 m and vent diameters of ~40 m. Conduits with larger vents generate decompression rates and mass fluxes too high for the Gray phase, whereas conduits with wider bases appear unreasonable given the size of Ksudach Caldera V.

A geologically reasonable interpretation of the Conflow results is that the eruption was fed by a broad conduit that became constricted near the top prior to and during caldera collapse. The modeling results suggest that a conduit with a basal diameter of ~400 m and an upper region constricted to ~100 m length scale could have fed the Main phase of eruption. Through this phase, the constricted length scale of the conduit likely remained 75–100 m. As the eruption progressed, the conduit geometry likely evolved through erosion of the upper regions and foundering of the base into the emptying chamber. Foundering of the base of conduit base, however, weakened the volcanic edifice, such that caldera collapse began during the Lithic phase of eruption. At the culmination of the Lithic phase, enough of the edifice foundered into the two-thirds empty chamber that the conduit base widened, but collapse further constricted upper regions of the conduit to ~60 m. Effectively, the collapsed upper region of the chamber became the conduit base. Comparison of the volume of lithics ejected by the start of the Gray phase, ~1 km^3, compared with Gray phase conduit volumes as suggested by Conflow, 1.5 to 2 km^3, suggest that foundering of <1 km^3 of the edifice is required for this model to be possible. Given that the Ksudach edifice collapsed during the KS_1 eruption to form a caldera, it should not be surprising that some of the collapse involved foundering of the edifice into the chamber.

Our scenario for the KS_1 eruption and caldera collapse describes the observed changes in mass flux and decompression rate. We propose that prior to eruption, pressure built in the chamber, fracturing the wall rock until a fracture propagated to the surface to become the eruption conduit. Further fracturing of wall rock along the conduit and the roof of

the chamber occurred during pre-collapse phases of eruption. Collapse began during the Lithic phase, as the weakened roof of the chamber and lower regions of the conduit broke apart and foundered or were ejected. Although the 0.3 km^3 of lithics ejected during the Lithic phase represents only ~25% of the total amount of erupted lithics, they were erupted at a rate 3–10 times greater than during any other phase of eruption. That substantial increase in lithic eruption rate reflects the fracturing that occurred as the edifice began to collapse. Importantly, however, only 20–33% of the lithics composing the developing Gray phase conduit were ejected during the Lithic phase; the remaining 0.5–1 km^3 foundered into the emptying chamber. Caldera collapse thus resulted in a conduit with a wider base and narrow top and a >75% reduction in decompression rate.

Supplementary materials related to this article can be found online at doi:10.1016/j.jvolgeores.2010.08.021.

Acknowledgements

The authors wish to thank P.E. Izbekov for conducting early phase equilibria experiments at UAF and his analyses of Fe–Ti oxides. V. Ponomareva, I. Melekestsev, and O. Selyangin of the Institute of Volcanology and Seismology in Petropavlovsk–Kamchatsky provided logistical assistance and field guiding. This project was partially funded by a grant from the National Science Foundation (EAR-0711043) to J.G. and through funding from the Alaska Volcano Observatory. Additional support was provided by the Jackson School of Geosciences. Thoughtful reviews by P.E. Izbekov and one anonymous reviewer significantly improved this manuscript.

References

Anderson, D.J., Lindsley, D.H., 1988. Internally consistent solution models for Fe–Mg–Mn–Ti oxides. Am. Mineral. 73, 714–726.
Anderson, D.J., Lindsley, D.H., Davidson, P.M., 1993. QUILF: a Pascal program to assess equilibria among Fe–Mg–Mn–Ti oxides, pyroxenes, olivine, and quartz. Comput. Geosci. 19, 1333–1350.
Andrews, B.J., Gardner, J.E., Tait, S., Ponomareva, V., Melekestsev, I.V., 2007. Dynamics of the 1800 ^{14}C yr BP caldera-forming eruption of Ksudach Volcano, Kamchatka, Russia. Geophys. Monogr. 172, 325–342.
Bacon, C.R., 1983. Eruption history of Mount Mazama and Crater Lake caldera, Cascade Range, U.S.A. J. Volcanol. Geotherm. Res. 18, 57–115.
Bacon, C.R., Hirschmann, M.M., 1988. Mg/Mn partitioning as a test for equilibrium between coexisting Fe–Ti oxides. Am. Mineral. 73, 57–61.
Bindeman, I.N., Leonov, V.L., Izbekov, P.E., Ponomareva, V.V., Watts, K.E., Shipley, N.K., Perepelov, A.B., Bazanova, L.I., Jicha, B.R., Singer, B.S., Schmitt, A.K., Portnyagin, M.V., Chen, C.H., 2010. Large-volume silicic volcanism in Kamchatka: Ar–Ar and U–Pb ages, isotopic, and geochemical characteristics of major pre-Holocene caldera-forming eruptions. J. Volcanol. Geotherm. Res. 189, 57–80.
Braitseva, O.A., Melekestsev, I.V., Ponomareva, V.V., Kirianov, V.Yu., 1996. The caldera-forming eruption of Ksudach volcano about cal. A.D. 240: the greatest explosive event of our era in Kamchatka, Russia. J. Volcanol. Geotherm. Res. 70, 49–65.
Browne, B.L., Gardner, J.E., 2006. The influence of magma ascent path on texture, mineralogy, and formation of hornblende reaction rims. Earth Planet. Sci. Lett. 246, 161–176.
Carey, S., Sparks, R.S.J., 1986. Quantitative models of the fallout and dispersal of tephra from volcanic eruption columns. Bull. Volcanol. 48, 109–125.
Druitt, T.H., Sparks, R.S.J., 1984. On the formation of calderas during ignimbrite eruptions. Nature 310, 679–681.
Gardner, J.E., Tait, S., 2000. The caldera-forming eruption of Volcano Ceboruco. Mex. Bull. Volcanol. 62, 20–33.
Gardner, J.E., Thomas, R.M.E., Jaupart, C., Tait, S., 1996. Fragmentation of magma during Plinian volcanic eruptions. Bull. Volcanol. 58, 144–162.
Hammer, J.E., Cashman, K.V., Hoblitt, R.P., Newman, S., 1999. Degassing and microlite crystallization during pre-climactic events of the 1991 eruption of Mt. Pinatubo, Philippines. Bull. Volcanol. 60, 355–380.
Hildreth, W., 1983. The compositionally zoned eruption of 1912 in the valley of Ten Thousand Smokes, Katmai National Park, Alaska. J. Volcanol. Geotherm. Res. 18, 1–56.
Hildreth, W., Mahood, G.A., 1986. Ring-fracture eruption of the Bishop Tuff. Geol. Soc. Am. Bull. 97, 396–403.
Hinch, E.J., Acrivos, A., 1980. Long slender drops in a simple shear flow. J. Fluid Mech. 98, 305–328.
Izbekov, P.E., Gardner, J.E., Andrews, B., Ponomareva, V.V., Melekestev, I.V., 2003. Petrology of Holocene caldera-forming eruptions at Ksudach, Kamchatka. EOS Trans. AGU 84 (46), V42B–V0347B Fall Suppl.
Jaupart, C., 2000. Magma ascent at shallow levels. In: Sigurdsson, H., Houghton, B.F., McNutt, S.R., Rymer, H., Stix, J. (Eds.), Encylopedia of Volcanoes, pp. 237–248.
Lipman, P.W., 2000. Calderas. In: Sigurdsson, H., Houghton, B.F., McNutt, S.R., Rymer, H., Stix, J. (Eds.), Encylopedia of Volcanoes, pp. 643–662.
Mangan, M., Sisson, T., 2005. Evolution of melt-vapor surface tension in silicic volcanic systems: experiments with hydrous melts. J. Geophys. Res. 110, B01202. doi:10.1029/2004JB003215.
Mastin, L.G., 2002. Insights into volcanic conduit flow from an open-source numerical model. Geochem. Geophys. Geosyst. 3 (7). doi:10.1029/2001GC000192.
Mastin, L.G., Ghiorso, M.S., 2000. A numerical program for steady-state flow of magma–gas mixtures through vertical eruption conduits. USGS Open-File Report 00-209.
Moore, G., Vennemann, T., Carmichael, I.S.E., 1998. An empirical model for the solubility of H_2O in magmas to 3 kilobars. Am. Mineral. 83, 36–42.
Newman, S., Stolper, E.M., Epstein, S., 1986. Measurements of water in rhyolitic glasses: calibration of an infrared spectroscopic technique. Am. Mineral. 71, 1527–1541.
Pallister, J.S., Hoblitt, R.P., Meeker, G.P., Knight, R.J., Siems, D.F., 1996. Magma mixing at Mount Pinatubo: petrographic and chemical evidence from the 1991 deposits. In: Newhall, C.G., Punongbayan, R.S. (Eds.), Fire and Mud: Eruptions and Lahars of Mount Pinatubo, Philippines, pp. 687–731.
Roche, O., Druitt, T.H., 2001. Onset of caldera collapse during ignimbrite eruptions. Earth Planet. Sci. Lett. 191, 191–202.
Rust, A.C., Manga, M., 2002. Bubble shapes and orientations in low Re simple shear flow. J. Colloid Interface Sci. 249, 476–480.
Scott, W.E., Hoblitt, R.P., Torres, R.C., Self, S., Martinez, M.M.L., Nillos Jr., T., 1996. Pyroclastic flows of the June 15, 1991, climactic eruption of Mount Pinatubo. Fire and Mud, pp. 545–570.
Sigurdsson, H., Carey, S., 1989. Plinian and co-ignimbrite tephra fall from the 1815 eruption of Tambora volcano. Bull. Volcanol. 51, 243–270.
Spera, F.J., 2000. Physical properties of magmas. In: Sigurdsson, H., Houghton, B.F., McNutt, S.R., Rymer, H., Stix, J. (Eds.), Encylopedia of Volcanoes, pp. 171–190.
Stolper, E.M., 1982. Water in silicate glasses; an infrared spectroscopic study. Contrib. Mineral. Petrol. 81, 1–17.
Stormer, J.C., 1983. The effects of recalculation on estimates of temperature and oxygen fugacity from analyses of multicomponent iron–titanium oxides. Am. Mineral. 68, 586–594.
Suzuki-Kamata, K., Kamata, H., Bacon, C.R., 1993. Evolution of the caldera-forming eruption at Crater Lake, Oregon, indicated by component analysis of lithic fragments. J. Geophys. Res. 98, 14059–14074.
Wilson, C.J.N., Hildreth, W., 1997. The Bishop Tuff: new insights from eruptive stratigraphy. J. Geol. 105, 407–439.
Zhang, Y., Belcher, R., Ihinger, P.D., Wang, L., Xu, Z., Newman, S., 1997. New calibration of infrared measurement of dissolved water in rhyolitic glasses. Geochim. Cosmochim. 61, 3089–3100.